



LAPP-EXP-97.05

## A Large Area Transition Radiation Detector for the NOMAD Experiment

G. Bassompierre<sup>a</sup>, M. Bermond<sup>a</sup>, M. Berthet<sup>a</sup>, T. Bertozzi<sup>a</sup>,  
C. Détraz<sup>b</sup>, J-M. Dubois<sup>a</sup>, L. Dumps<sup>b</sup>, C. Engster<sup>b</sup>, T. Fazio<sup>a</sup>,  
G. Gaillard<sup>a</sup>, J-M. Gaillard<sup>a</sup>, M. Gouanère<sup>a</sup>,  
E. Manola-Poggioli<sup>a,1</sup>, L. Mossuz<sup>a</sup>, J-P. Mendiburu<sup>a</sup>,  
P. Nédélec<sup>a,1</sup>, E. Palazzini<sup>a</sup>, H. Pessard<sup>a,2</sup>, P. Petit<sup>b</sup>,  
P. Petitpas<sup>a</sup>, A. Placci<sup>b</sup>, D. Sillou<sup>a</sup>, R. Sottile<sup>a</sup>, V. Valuev<sup>a,c,1</sup>,  
D. Verkindt<sup>a</sup>, H. Vey<sup>a</sup>, M. Wachnik<sup>b</sup>.

<sup>a</sup>LAPP, Laboratoire d'Annecy-le-Vieux de Physique des Particules, IN2P3-CNRS,  
BP 110, F-74941 Annecy-le-Vieux CEDEX France

<sup>b</sup>CERN, European Laboratory for Particle Physics, CH-1211 Geneva 23,  
Switzerland

<sup>c</sup>JINR, Joint Institute for Nuclear Research, 141980 Dubna, Moscow region,  
Russian Federation

A Transition Radiation Detector to identify electrons at 90% efficiency with a rejection factor against pions of  $10^3$  on an area of  $2.85 \times 2.85 \text{ m}^2$  has been constructed for the NOMAD experiment. Each of its 9 modules includes a 315 plastic foil radiator and a detector plane of 176 vertical straw tubes filled with a xenon-methane gas mixture. Details of the design, construction and operation of the detector are given.

*PACS:* 29.40.Ym; 07.85.Yk; 14.60.Pq

*Key words:* Transition radiation detector; electron identification; neutrino oscillations.

<sup>1</sup> Now at European Laboratory for Particle Physics (CERN), CH-1211 Geneva 23, Switzerland

<sup>2</sup> Corresponding author. Tel.: (+33) 04 50 09 16 08; fax: (+33) 04 50 27 94 95; e-mail: pessard@lapp.in2p3.fr

Preprint submitted to Elsevier Preprint

10 July 1997



Sw 9749

## 1 The NOMAD experiment

NOMAD [1] is a search for  $\nu_\mu \rightarrow \nu_\tau$  oscillations in the wide-band neutrino beam of the CERN SPS. The appearance of  $\nu_\tau$  will be detected through their charged-current interactions that have to be extracted from a background of about  $1.5 \times 10^6$   $\nu_\mu$  charged-current and neutral-current interactions. As the selection of  $\tau^-$  decays relies upon kinematical criteria applied to the reconstructed events, a low density active target is used for accurate measurements of the interaction products. This gives the possibility to reconstruct electron tracks.

The semileptonic decay of a  $\tau^-$  into an electron  $\tau^- \rightarrow e^- + \bar{\nu}_e + \nu_\tau$  is one of the most sensitive signatures for the neutrino oscillation search, provided a rejection factor of at least  $10^5$  is achieved against pions when identifying electrons. This rejection factor is needed to eliminate neutral-current background events in which an isolated pion simulates an electron.

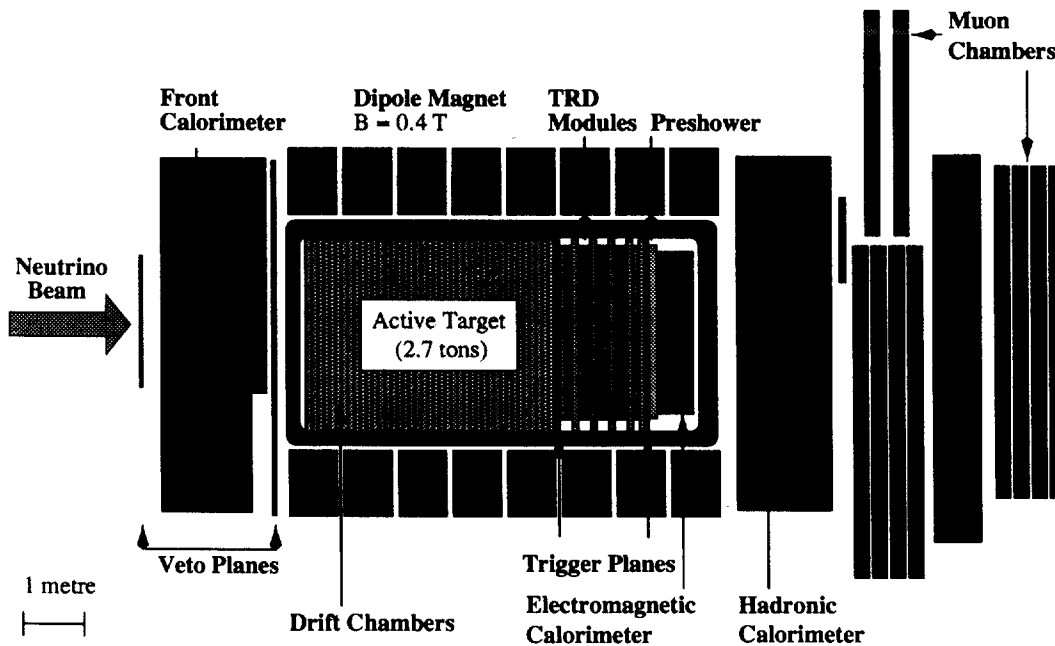


Fig. 1.1. Schematic side view of the NOMAD detector

The central part of the NOMAD detector is housed in a magnet of internal dimensions  $7.1 \times 3.5 \times 3.5 \text{ m}^3$  (the former UA1 magnet). The magnetic field, horizontal and perpendicular to the beam direction, is set to 0.4 Tesla. Most of the space is taken by a set of drift chambers, which act both as the neutrino

target and as a tracking detector. Downstream of the drift chambers are placed the electron detectors: a transition radiation detector (TRD), located between two trigger planes, followed by a preshower and a lead-glass calorimeter (see Figure 1.1). A muon detector system is set up behind the magnet. The whole apparatus is described in Ref. [2].

The NOMAD TRD was designed to identify electrons with 90% efficiency while providing a pion rejection factor of  $10^3$  in a momentum range 1 to 50 GeV/c. In conjunction with the preshower and the electromagnetic calorimeter downstream of the TRD, a total rejection factor of  $10^5$  against pions is reached since the rejection factors from the TRD and calorimeter systems are to first order multiplicative.

The TRD is made of individual modules, consisting of a radiator followed by a detector plane. Within the longitudinal space available (154 cm), a total of 9 TRD modules have been implemented, interspersed with 5 drift chambers to measure the tracks through the TRD up to the calorimeter.

The total amount of material within a TRD module (mostly that of its radiator) was limited to 0.01 radiation length ( $X_0$ ) so that there is at most  $0.02 X_0$  between two drift chambers in the TRD section. In addition, the bulk of the detector frame had to be minimized in the mechanical design to keep a large active area.

The rejection factor required and the dimensions of its active area ( $2.85 \times 2.85 \text{ m}^2$ ) make the NOMAD TRD one of the largest TRD with high pion rejection ever built [3].

## 2 The design of the TRD detector

### 2.1 General principles

The transition radiation effect [4,5] is an efficient way to separate electrons from other charged particles in the NOMAD momentum range.

Transition Radiation (TR) is produced by charged particles crossing boundaries between media of different electron densities. The TR energy radiated at an interface and the number of TR photons are proportional to the Lorentz factor  $\gamma = E/m$  of the particle, so this effect can be used for particle identification. However, the emission probability of a photon is small (of the order of  $\alpha = 1/137$ ) and in practice a "radiator" with many interfaces is used. The

detectable amount of TR energy is then reduced by the absorption of the TR photons, which are in the keV range, in the radiator material and the coherent effect is limited by dispersions in the regular spacing of the interfaces [6,7].

To affect minimally the incident particle, a gaseous detector is chosen to detect the emitted X-rays. The gas used is xenon which has a high Z and photo-absorption peaks in the energy range of the TR photons (see Figure 2.1).

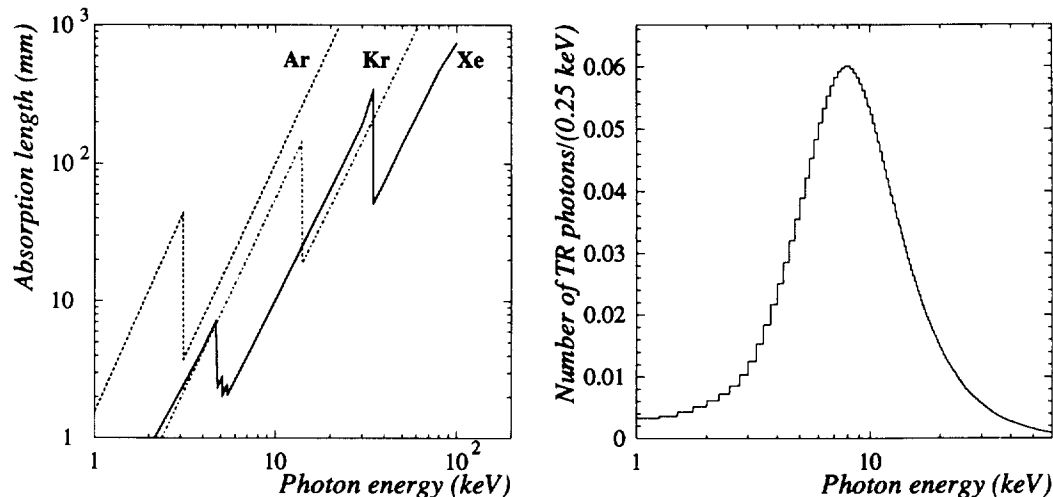


Fig. 2.1. Left: Absorption length of photons in various rare gases as a function of photon energy. Right: Transition radiation spectrum produced by 5 GeV electrons at normal incidence in a NOMAD TRD radiator.

Due to the small angle of X-ray emission ( $\sim 1/\gamma$ ), the TR energy deposition is mixed with the simultaneous ionization loss from the parent particle in the detector gas. In practice, TRDs detect TR energies of the same order of magnitude as the accompanying  $dE/dx$ . As an example, a 10 GeV/c electron crossing a NOMAD radiator at normal incidence produces on average 3.1 photons of mean energy 14 keV. About 1.5 photons of mean energy 8 keV are detected, leading to a detected TR energy of  $\sim 12$  keV. The superimposed ionization losses of the electron amount to  $\sim 9$  keV. Due to large fluctuations of both TR and  $dE/dx$ , consecutive measurements are needed to achieve efficient identification.

The NOMAD TRD consists of 9 identical modules, each composed of a radiator followed by a detection plane. A radiator is a set of polypropylene foils  $2.85 \times 2.85$  m<sup>2</sup> in area. A detection plane consists of 176 adjacent vertical straw tubes of 16 mm diameter, operating in the proportional mode with a Xe - CH<sub>4</sub> gas mixture. The first 8 modules are paired into 4 doublets (see Figure 2.2). Five tracking drift chambers are embedded in the TRD, one after each doublet and one after the last module. The following sections describe the technical choices and the construction of the TRD.

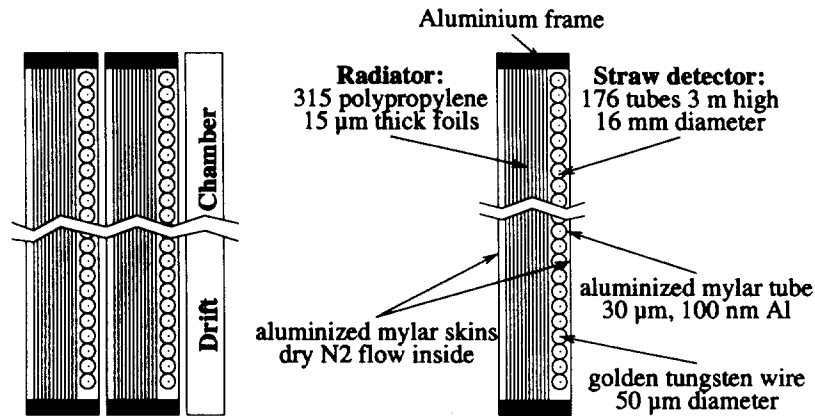


Fig. 2.2. The pairing of TRD modules and their structure (top view)

## 2.2 The TRD radiators

### 2.2.1 Radiator materials

The best candidates are high density low  $Z$  materials, since photon reabsorption in the radiator grows like  $Z^4$ . The best choice would be lithium, but it is difficult to use in practice and plastics  $(CH_2)_n$  are most convenient to manufacture large dimensions radiators. They can be used under the form of foam or fiber blocks (mechanically preferable as a strong supporting frame is not needed) or, alternatively, as a thin foil structure. Studies made in the past [8] to compare the transition radiation produced in different forms of radiators have shown that thin foil radiators are more efficient for a given radiator thickness.

We have performed several measurements with test-beams and reached the same conclusions, although the detection was not optimal due to gas impurities in the photon detector. Figure 2.3 is an example of such a measurement where a polyethylene foam block of 3.1% radiation length and 235 mm thick was compared to a 500-foil test radiator containing less matter (2.3% radiation length and 210 mm thick). The result, 30% more energy detected in the second case, clearly favours the foil radiator. We have finally chosen polypropylene foils (mechanically easier to stretch than polyethylene foils).

In between foils, vacuum would be the best but is not practicable. We use nitrogen gas which has a reasonably low plasma frequency and is easier to use than helium for gas-tightness reasons.

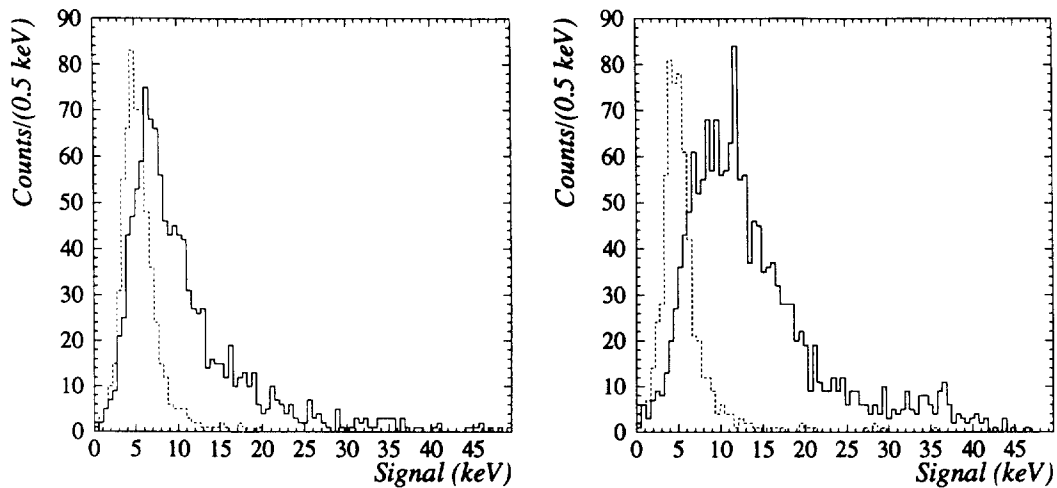


Fig. 2.3. Detected response to electrons in a 2 GeV/c test-beam with a foam radiator (left) and with a 500-foil radiator (right). Dotted lines show the response to pions.

### 2.2.2 Radiator structure, TRD modularity

Simulation programs [9] were used to compute the number of detected TR photons emerging from radiators up to  $0.01 X_0$  thick with uniformly spaced foils and a given length. The number of foils, their thickness and the gap were varied. Figure 2.4 shows the result of such a calculation. The effects of

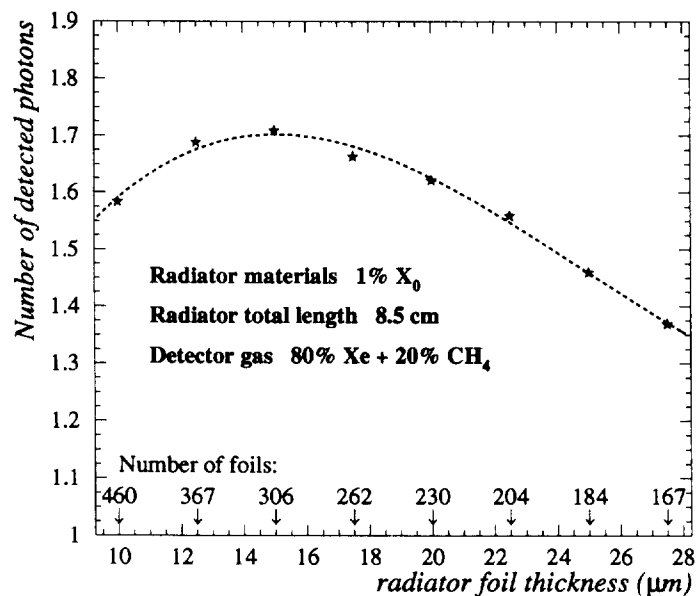


Fig. 2.4. Number of detected TR photons as a function of the radiator foil thickness, for given radiator length and allowed amount of material. The curve shown results from a smoothing algorithm.

foil thickness and gap dispersions were included in the computations and the

results were checked by test-beam measurements.

As a result of simulation and test-beam studies, the detector consists of 9 modules, with radiators made of 315 polypropylene foils, each  $15\ \mu\text{m}$  thick, spaced by  $250\ \mu\text{m}$ .

## *2.3 The detection planes*

### *2.3.1 Choice of a straw detector for the transition radiation*

A large planar detector filled with xenon gas would require a thick window which would absorb low-energy transition radiation photons. Therefore the counter was made of vertical cylindrical tubes ("straws") with  $28\ \mu\text{m}$  aluminized mylar walls, placed side by side. The straw diameter,  $16\ \text{mm}$ , was chosen to have a high probability for capturing the transition radiation while keeping the ionization loss due to the particle crossing the tube at a reasonably low level.

Cylindrical straws introduce a variation of the gas thickness traversed by a particle, depending on track position. The mean efficiency of a TRD straw plane has been estimated to  $\sim 98.5\%$  for minimum ionizing particle tracks. The detector response as a function of the track position is further discussed in section 7.2.3.

A vertical or horizontal orientation of the straws could a priori be considered. The vertical orientation was preferred for wire electrical stability. The anode wire should be kept within close distance from the straw axis (see section 2.3.3). An horizontal orientation would have required spacers because of straw gravitational sagging, thus introducing dead zones within the active area of the detector.

We have chosen to measure the total energy deposition in the straw detector and to operate the detector in proportional mode. The methods of "cluster counting" reach the same rejection power as the total energy deposition method [8]. Using a defined threshold is however difficult in our case due to space charge effects, which depend upon the track angle as discussed later in this paper, whereas charge integration leaves more flexibility in the off-line treatment.

### 2.3.2 Detector gas mixture

The gas mixture chosen for the proportional detector of the TRD is made of 80% Xe, 20% CH<sub>4</sub>:

- xenon offers the largest absorption cross-section for the transition radiation photons, as shown in Figure 2.1.
- methane, at the level of 20%, gives a much shorter drift time than carbon

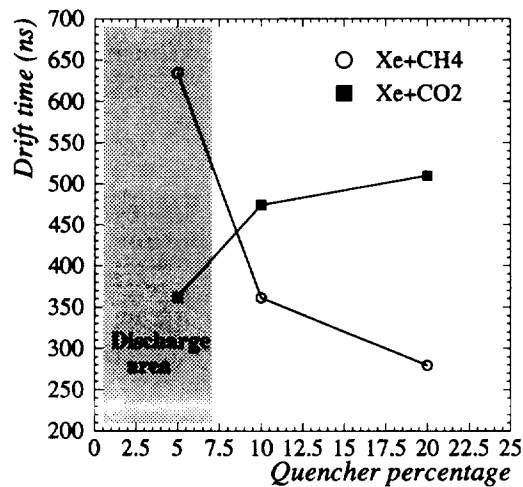


Fig. 2.5. Total drift time in TRD straws versus the percentage of CH<sub>4</sub> or CO<sub>2</sub> in Xenon.

dioxide, as shown in figure 2.5 obtained using published data [10] for a constant gain around 6000 with a 50  $\mu\text{m}$  wire diameter (for example 20% CH<sub>4</sub> and HV=2200Volts). This shorter drift time for Xe-CH<sub>4</sub> leads to a lesser sensitivity to impurities such as oxygen or nitrogen.

Our simulations have shown that pion/electron rejection is not significantly influenced for CH<sub>4</sub> percentage values between 10% and 40%, at constant gain. The CH<sub>4</sub> percentage of 20% was chosen to keep the high voltage at a relatively low value.

### 2.3.3 Straw wire diameter and mechanical tension

The stability of the central wire in a cylindrical straw depends on its mechanical tension  $T$  and on the high voltage  $V$ . The stability condition for a centered



wire<sup>3</sup> is:

$$V^2 \leq T \frac{\pi R^2 [\ln(\frac{R}{r})]^2}{2\epsilon_0 L^2} = V_0^2 \quad (2.1)$$

where L is the wire length, R the straw radius and r the wire radius. If the wire is shifted by  $\Delta$  from the straw axis, the amplitude of the wire deflection is:

$$A = \frac{\pi \Delta}{2(\frac{V_0^2}{V^2} - 1)} \quad (2.2)$$

We have compared two different wire diameters, 20  $\mu\text{m}$  and 50  $\mu\text{m}$ , at a gain value of  $1.5 \cdot 10^4$ . With a 80%-20% Xe-CH<sub>4</sub> gas mixture, that gain was reached at 1800 (2300) Volts with a 20 (50)  $\mu\text{m}$  wire, respectively. Assuming a maximum displacement  $\Delta$  of 0.5 mm away from the axis, if one requires the deflection A not to exceed 0.5 mm, the mechanical tensions needed for 20  $\mu\text{m}$  and 50  $\mu\text{m}$  tungsten wires are then 15 g and 33 g, as indicated in Table 1.

H.V.	diam.	needed tension	breaking limit
1800 V	20 $\mu\text{m}$	15 g	60 g
2300 V	50 $\mu\text{m}$	33 g	300 g

Table 1  
Properties of two different diameters for tungsten wires.

As seen from this table, the safety margin is better with a 50  $\mu\text{m}$  wire. As the drift velocity is higher [10], the sensitivity to impurities is also reduced. The maximum drift time is 303 ns with a 20  $\mu\text{m}$  wire and 270 ns with a 50  $\mu\text{m}$  wire. For a 80%-20% Xe-CO<sub>2</sub> gas mixture, this difference would have been much larger: 900 ns for a 20  $\mu\text{m}$  wire and 525 ns for a 50  $\mu\text{m}$  wire. One could, in principle, increase the wire diameter even more. However, in order to limit the high-voltage, a 50  $\mu\text{m}$  diameter gold-plated tungsten wire<sup>4</sup> was chosen. With a tension of 100 g at 2300 V, its distance to the straw axis is at most 0.61 mm assuming a shift  $\Delta$  of 0.5 mm.

<sup>3</sup> H. Ogren *et al.*, "Wire stability tests on 4mm straw chambers", note SDC-90-00055

<sup>4</sup> Gold-plated tungsten 50  $\mu\text{m}$  diameter wire Lumalampan 861/60.

### 3 The construction of the TRD modules

#### 3.1 Construction of the frames

The frames of the TRD must stand the mechanical tensions from the TRD radiator foils (315 foils at 2 kg tension in each direction) and from the straw tubes (176 straws at 300 g and 176 wires at 100 g).

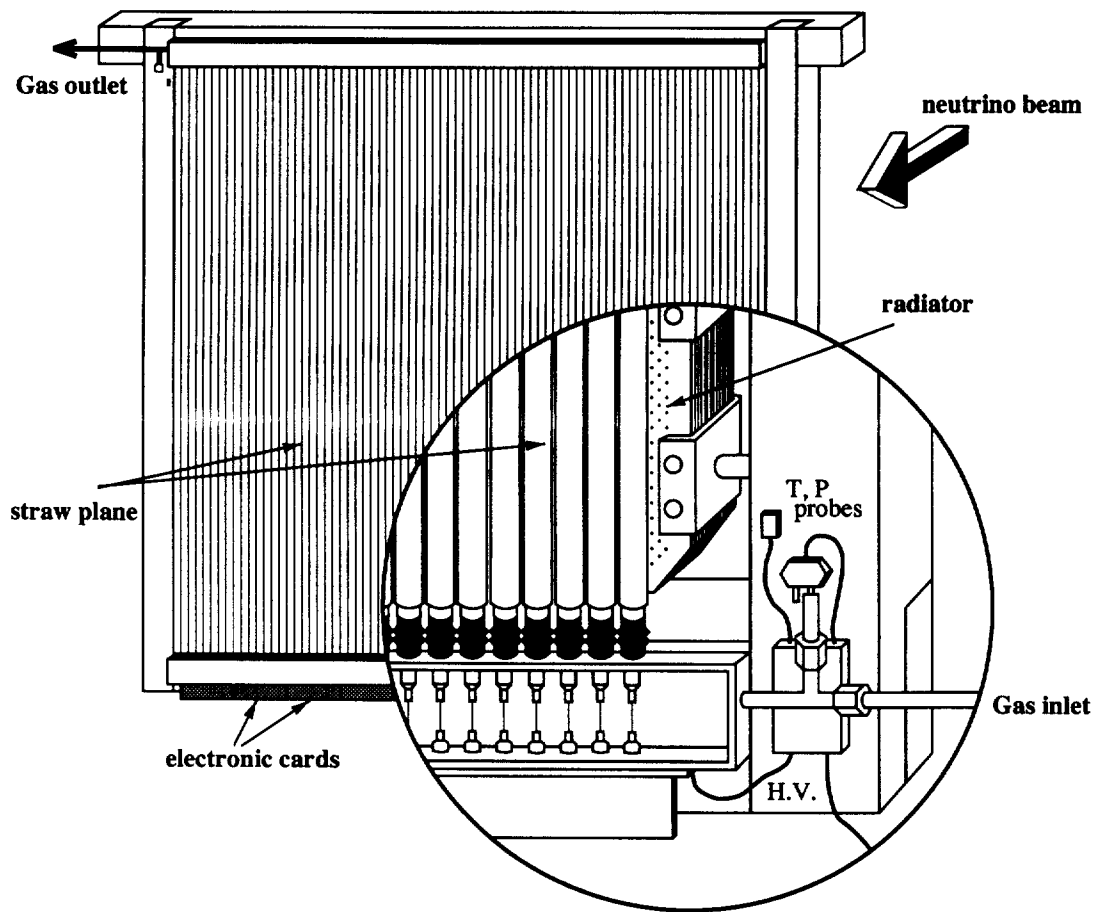


Fig. 3.1. Simplified view of a TRD module frame. The detail of the bottom right corner depicts the fixation of the straws and radiator foils, and shows the location of various sensors.

The frames are made of 4 solid aluminium girders in which 17 holes are drilled to pull with springs the radiator tensioning rods terminated by clamps holding the radiator foils (see Figures 3.1 and 3.2). The top and bottom girders which support the gas distribution volumes holding the straws are 117 mm thick including 3 mm thick covers. The frames have an internal area

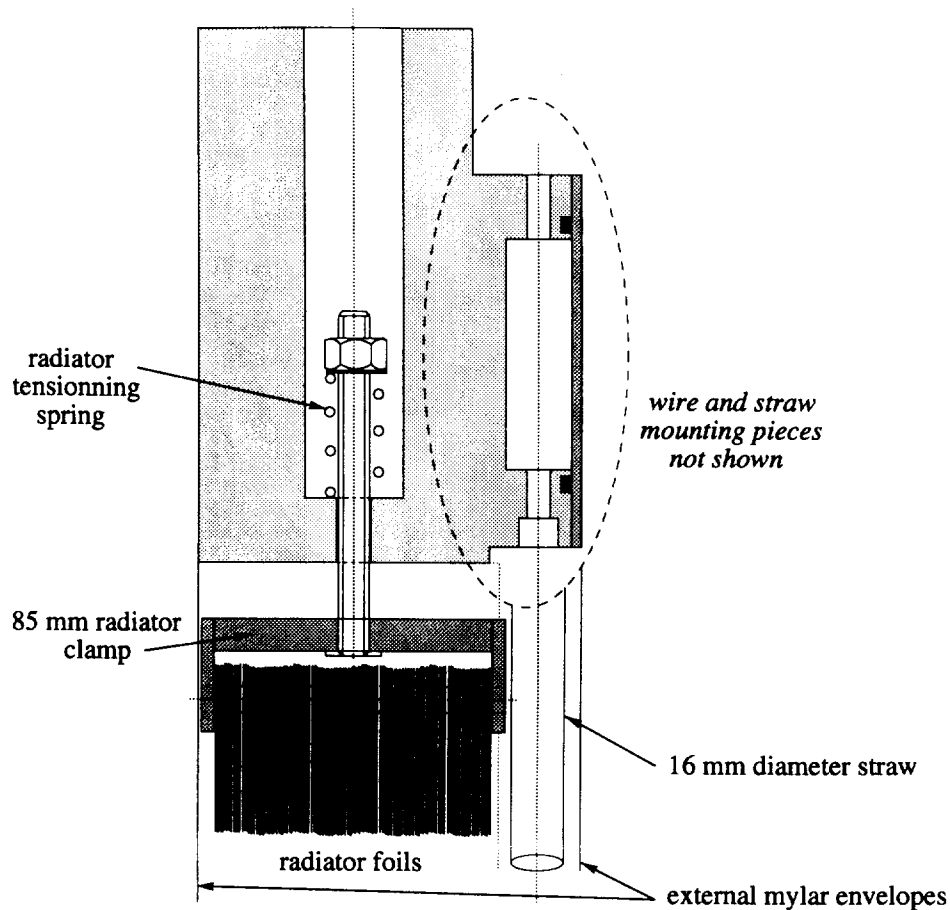


Fig. 3.2. Assembly of the radiator in the TRD frame (cut view). Details of the straw tubes mounting are shown in Figure 3.5

of  $2930 \times 2930 \text{ mm}^2$ . With the radiators and the straws, the sagitta of the frames on the 3 meters span is less than 1.5 mm.

### 3.2 Radiators

The spacing of radiator foils should be as regular as possible not to decrease the amount of emitted transition radiation. To keep a uniform gap between foils on their whole area, the polypropylene film is first embossed with  $250 \mu\text{m}$  bumps. Shifted lines of bumps distant by 50 mm are made every 20 mm. Bumps amount to 1/1000th of the foil area. A special machine has been designed and built (see Figure 3.3) to thermoform the bumps by imprinting the form of steel moulds on the foils, using hot-air nozzles. The rate of production was 12-15 m/hr.

Radiator foils are held to the frame by 17 clamps on each of their four sides.

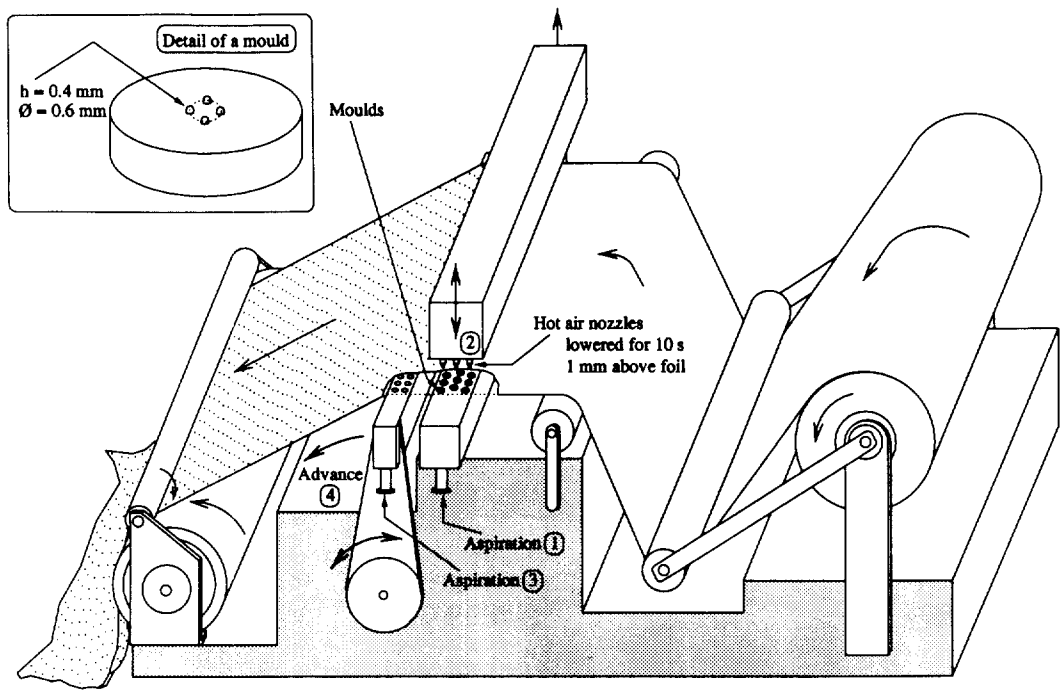


Fig. 3.3. Principle of the radiator foil embossing machine (not to scale).

The radiator is prepared on a specially designed table (see Figure 3.4) where

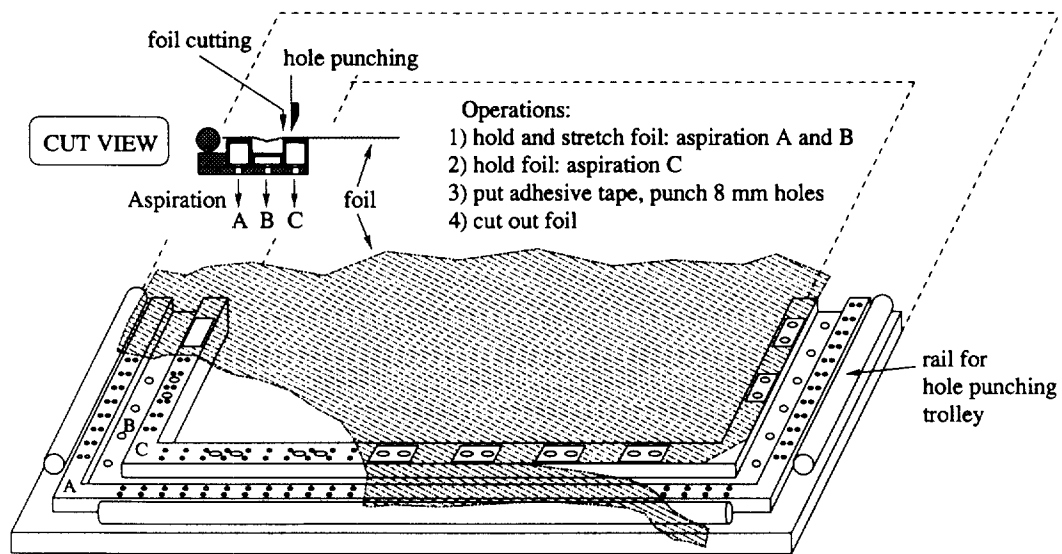


Fig. 3.4. Schematic view of the radiator preparation table.

each foil is first stretched in place by a vacuum system located on its outside perimeter. Holes intended for the clamp rods are punched in the foil, which has been locally reinforced by a piece of adhesive tape  $250 \mu\text{m}$  thick. These tapes set the interfoil gap. The foils, successively mounted on the clamp rods, are eventually introduced as a stack in the detector frame, and the tension is

then applied to the clamp springs.

### 3.3 Assembly of the straw planes

The straw tubes [11] are made of two 16 mm wide ribbons of 12.5  $\mu\text{m}$  thick terphane<sup>®</sup>, shifted by 8 mm and wrapped in an helix around a 16 mm diameter rod. The ribbons are glued together during the wrapping. The ribbon inside the straw is coated with 115 nm aluminium to act as the tube cathode. The total tube wall thickness is 28  $\mu\text{m}$ .

The vertical straws are stretched at a tension of  $\sim 300$  g by springs linked to the frame (see Figure 3.5) in order to cope with their length fluctuations due to temperature. For the wires, as their elasticity stands the effect of large temperature variations, they are rigidly attached to the frame.

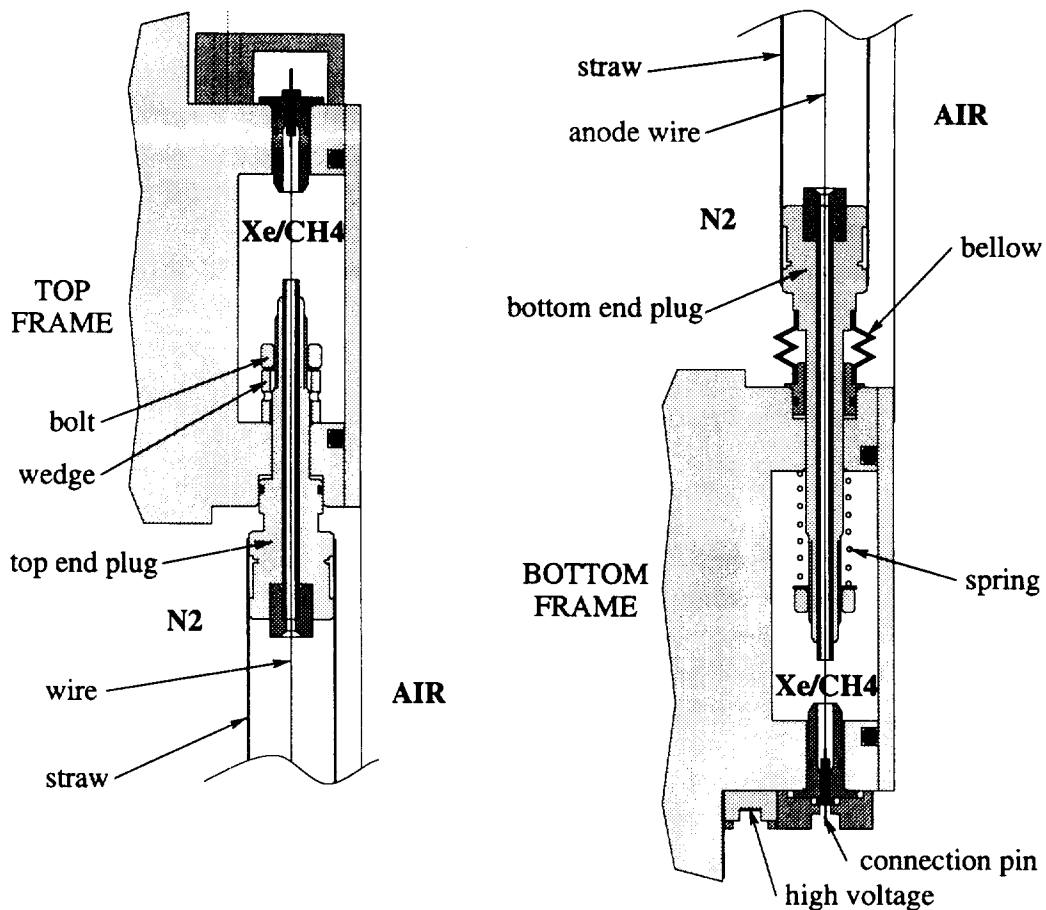


Fig. 3.5. Assembly of the straws and wires in the TRD frame (top and bottom cut views).

Metallic straw end-plugs were designed to connect electrically the straws to the frame. The plugs are glued inside the aluminized straw with a small amount (0.6 g) of conductive glue<sup>5</sup>. Plastic parts allowing gas circulation insulate the wire feed-through (insulating parts are shown in darker gray in Figure 3.5). For gas-tightness, O-rings are used in the mounting and each straw is equipped with a Viton bellow allowing straw shifts relative to the frame.

Straws were first cut to size and glued to their end-plugs on specially designed tables. Even vertical, free straws are not naturally straight enough over a 3 m length, and as much as 500 g mechanical tension was needed to straighten the thin tubes. However, as the straws were stretching (at a rate of 0.57 mm per month) when submitted to a 500 g tension, an alternative procedure was followed. The straws, equipped with their bellows and inflated at 1.3 atm, were hanged vertically using special fixtures, each with a 7 kg weight for 12 hours. Straws were then allowed to rest for 7 days. This operation, combined with the final tension of 300 g, yielded enough stability. After this prestressing procedure, the straws were mounted on the TRD frames. The wires were then threaded through the straws using a special machine and crimped at their nominal 100 g tension.

The cost of xenon makes gas tightness very important. Thus a limit for the pressure drop of a completed straw was set at 1 g/hour at 300 g overpressure. A test system was set up to check the straws for leaks during their prestressing phase and when mounted. We achieved an average pressure drop per TRD module of 0.47 g/hour at 300 g overpressure. This corresponds to a total gas leak from the 9 chambers operating at 100 g overpressure of 160 cc/hour.

### 3.4 *External envelopes*

The permeability of the straw walls to the outside gases, such as oxygen and nitrogen, and to water vapour is also an important issue. Mylar has a very high permeability to water vapour, which is reduced by aluminization. To assess the problem, we performed measurements on 3 m long test straws whose aluminium coating was 40 nm thick.

At a N<sub>2</sub> flow of 10 cc/mn (1 volume/hour) through a single straw, contaminations of 30 ppm O<sub>2</sub> and 5300 ppm H<sub>2</sub>O from the air were measured. The water vapour contamination level was still 50% that of the ambient air. For a N<sub>2</sub> flow 50 times larger, completely excluded for the full detector, the water vapour contamination was decreased by a factor 35.

---

<sup>5</sup> Silver glue Eleco Products 336.

Other measurements were done with a 16-straw prototype whose frame apertures could be left open or closed with various mylar skins, to blow nitrogen around the straws at a rate of 0.35 vol/hr. An 80%Ar - 20%CH<sub>4</sub> gas mixture was circulated through the straws at 3 cc/mn per straw (0.33 vol/hr). The results of the measurements, given in Table 2, demonstrate the necessity of external envelopes.

Conditions	O <sub>2</sub>	H <sub>2</sub> O
No skins	216 ppm	11.000 ppm
25 μm mylar skins + N <sub>2</sub> at 500 cc/mn	82 ppm	7000 ppm
25 μm mylar skins, 25 nm Al coating + N <sub>2</sub> at 500 cc/mn	83 ppm	1000 ppm

Table 2  
Oxygen and water vapour contamination in different conditions.

In order to keep H<sub>2</sub>O and O<sub>2</sub> contaminations at reasonably low levels, each TRD module was sandwiched between two aluminized mylar skins (36 μm thick, 28 nm Al coating) between which nitrogen was flown. For a TRD module with a nitrogen flow set at 40 l/hr (0.25 vol/hr) and a Xe-CH<sub>4</sub> mixture flowing through the straws at a rate of 70 l/hr (0.6 vol/hr), the contamination increases typically by 20 ppm for O<sub>2</sub> and 100 ppm for H<sub>2</sub>O between the input and the output of the detector. This contamination is removed by the gas purification system.

#### 4 Gas circulation and purification system

The quality of the transition radiation signal requires:

- an excellent uniformity and stability of the Xe-CH<sub>4</sub> proportions within the whole detector.
- a low level contamination of the gas mixture, especially from oxygen and water.

A closed circuit system with continuous purification of the gas is used (see Figure 4.1). The gas mixture brought up to a pressure of 1 kg/cm<sup>2</sup> by a membrane compressor, is first sent through a palladium catalysor for O<sub>2</sub> elimination followed by a molecular sieve filter where water is trapped. The pressure is then lowered to 100 g/cm<sup>2</sup> and the gas is sent via separate copper lines to prevent

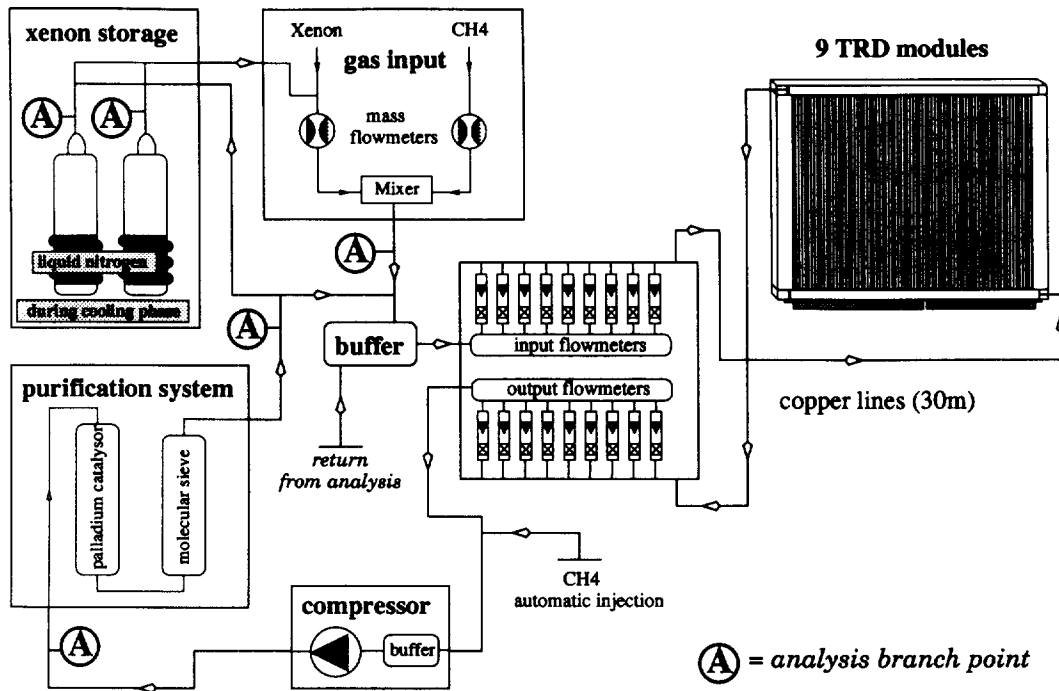


Fig. 4.1. Principle of the TRD gas system.

contamination by water to the bottom of each TRD plane with an adjustable flow.

For each plane, the 176 straws are fed in parallel from a lower buffer volume and the output gas is collected in an upper buffer (see Figures 3.5 and 3.1). The system was designed to provide an approximately equal gas impedance path for each straw. The  $\text{CH}_4$ ,  $\text{O}_2$  and water percentages are measured at any one of 5 points in the circuit via sampling loops.

#### 4.1 Operating conditions

The  $\text{Xe-CH}_4$  mixture is circulated through the detector at a rate of 600 l/h, about half the total volume of the detector. The gas losses of the system are compensated for in order to maintain both a constant total gas amount and a stable  $\text{Xe-CH}_4$  composition by:

- an input of Xe whose rate is automatically adjusted by the pressure level at the detector input. This addition amounts to about 10 liters per day.
- an intermittent injection of  $\text{CH}_4$  activated for a fixed duration when the  $\text{CH}_4$  percentage dropped by 0.5% with respect to the nominal value. The full range of the  $\text{CH}_4$  percentage variation is less than 1.0% under these



conditions.

#### *4.2 Fill and purge operations*

To fill the detector, the TRD and its gas system are first flushed with  $\text{CH}_4$  for 30 hours. Pure xenon is then introduced at a rate of about 50 l/h through the bottom of the detector so that it forces  $\text{CH}_4$  out to the top with little mixing between the two gases. The filling operation is monitored continuously by measuring the  $\text{CH}_4$  percentage at the output of the TRD planes. The system is switched to the closed circuit operation when the percentage is decreased to 30%, after about 15 hours. Fine adjustments of the gas composition take a few more hours.

For the purge operation, pure  $\text{CH}_4$  is introduced at the top of the detector pushing the Xe- $\text{CH}_4$  mixture out through the bottom into a 50 liter gas cylinder cooled down to liquid nitrogen temperature by an external jacket. Both Xe and  $\text{CH}_4$  are stored in a liquid form. The purge operation is also continuously monitored by measuring the  $\text{CH}_4$  percentage. When the operation is over, the bottle is first warmed up, then cooled down to an intermediate temperature of  $-110^\circ\text{C}$  where the  $\text{CH}_4$  gas is pumped out with only a few percent loss of the liquid Xe. This xenon bottle is used for the next fill of the detector.

### **5 Electronics**

The electronic chain amplifies and records the straw signals via ADCs. After preamplification by front-end cards placed just below the straw planes, the signals are sent to Fastbus receiver cards and then transmitted to Fastbus ADC cards.

Low activity  $^{55}\text{Fe}$  sources, placed in front of each TRD plane, generate calibration signals between the accelerator bursts. A logical level synchronized with the accelerator cycle allows to switch the receiver card to the calibration mode or to the external physics trigger mode. The electronic chain has also an internal calibration system using charge injection at the front-end preamplifiers level.

## 5.1 Choice of high-voltage and electronic gain

The choice of high-voltage and electronic gain is a compromise between non-linearity effects and electronic noise. For the whole detector, the pedestal width  $\sigma_{Ped}$  is generally  $\sim 3$  ADC counts, with maximum values not exceeding 6 ADC counts (see for example Figure 6.1). With the high-voltage set to 2225 Volts, a cut at  $5\sigma_{Ped}$  above the pedestal value, applied during the data taking, corresponds to less than 0.3% loss for minimum ionizing particles.

With a gas gain of  $\sim 0.7 \times 10^4$  at 2225 Volts and a preamplifier gain  $\sim 200$  the 5.89 keV  $^{55}\text{Fe}$  signal has an amplitude of  $\sim 20$  mV ( $\sim 250$  ADC counts). The discriminator threshold is set at 15 mV, just above the noise ( $\sim 10$  mV).

## 5.2 Front-end electronics

### 5.2.1 Front end cards

The 176 straws of each plane are organized in subsets of 16 straws through 11 front-end cards placed under the straw plane. Each front end card has the following functions:

- Amplification of the signals by 16 preamplifiers.
- Distribution of the high voltage to the straw wires. The card is connected to the 16 straw pins and to the copper high voltage bus by pump-connectors. The high voltage is transmitted via  $10M\Omega$  resistors.
- Connection of the wires to the preamplifiers. The connection is made through a 2.2 nF decoupling capacitor and a  $180\Omega$  resistor which matches the preamplifier to the iterative impedance of the straw.
- Connection to 32-pair output signal cables.
- Ground contact to the TRD aluminium frame.
- Injection of test-pulses as part of the electronic gain control system (see section 6.2).

### 5.2.2 Pre-amplifiers

The front-end card preamplifiers were built by Gatchina Electronic Labora-

tory<sup>6</sup> with the characteristics indicated in Table 3.

Differential gain	13.3 mV / $\mu$ A
Output impedance	50 $\Omega$
Rise time	< 10 ns
Power supply	+6 Volts (24 mW)
Noise	19.6 nA for a 100 ns gate width
Input impedance	50 $\Omega$
Non-linearity	< 1% up to 1200 mV
Decay time of AC coupling	> 7 $\mu$ s
Size	11 $\times$ 24 mm <sup>2</sup> (hybrid technology)

Table 3  
Parameters of the front-end card preamplifiers.

Preamplifiers and front-end cards were submitted to thermal cycles of 4 hours at  $-10^{\circ}\text{C}$  and 4 hours at  $+50^{\circ}\text{C}$  for a total of 72 hours. The preamplifier gain and linearity were then measured on a calibration chain.

### 5.3 Electronics acquisition Fastbus chain

#### 5.3.1 Analog signals

After preamplification, the electronic signal from each straw is output to a 31 meter twisted pair. Two 32-pair cables are connected via an auxiliary card to the backside of a Fastbus receiver card called "RECV". The 64 signals are delayed by 250 ns in order to be in time with the trigger. The analog output signals from a RECV card are connected to the adjacent Fastbus card, the "ADC" card, by a flat cable (see Figure 5.1). The length of this cable is kept to 5 cm for low noise pick-up and short ground connection between the RECV and ADC cards.

The 64-channel ADC cards were specially designed for NOMAD, with:

- a 1000 pC, 12 bit dynamical range,
- a 256 word memory,
- a total busy time of  $\sim 6 \mu\text{s}$ .

<sup>6</sup> Gatchina, St. Petersburg (Russian Federation).

The ADC card integrates the charge during the gate provided by the RECV card. The gate length is set to 500 ns, enough to collect most of the pulse coming from a straw and to take into account the fluctuations due to different distances of the tracks to the wire (250 ns).

The information of the 1584 straws in the experiment is collected by 3 Fastbus crates, each with 9 RECV cards and 9 ADC cards.

### 5.3.2 Logical signals: physics trigger and calibration trigger

Within a RECV card, triggers are defined by either an external physics trigger signal or by an internal calibration trigger enabled by a logical level. For every trigger, the RECV card delivers a 500 ns gate to the neighbouring ADC card through a short coaxial cable. The physics trigger and calibration enable signals are fed in parallel to all auxiliary RECV cards, via a flat cable acting as an input bus line. This bus line is also used to send other signals, described below, to the RECV cards, in order to select specific cards or channels for calibration.

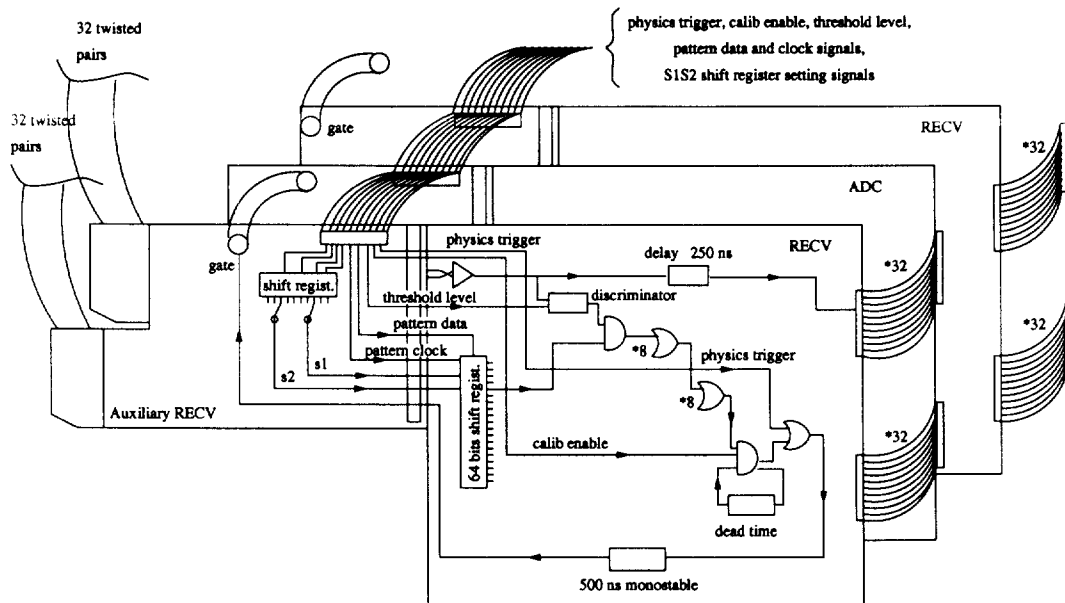


Fig. 5.1. Acquisition electronics

### The calibration trigger

The calibration triggers come from discriminators on each channel, with a common threshold, usually 15 mV, which is set by a threshold level delivered via the backside flat cable. A gate controlled by a pattern addressing system is placed after each discriminator to inhibit or activate the corresponding channel. The "OR" of the 64 gate outputs forms the calibration trigger. To

avoid pile-up, a  $6 \mu s$  dead time is imposed to the calibration trigger (see Figure 5.1). The "OR" of the calibration trigger and of the physics trigger is then used to create the 500 ns ADC gate.

### The calibration pattern addressing system

To address a given RECV card within a crate, the lines S1 and S2 of the auxiliary RECV card are connected via jumpers to the corresponding outputs of a 24-bits shift register which is controlled by signals sent through the backside flat cable. To allow the selection of channels for calibration, the outputs of a 64-bit shift register placed on each RECV card are connected to its 64 gates. To set a 64-channel calibration pattern, the signals S1 and S2 are set to the "shift left" mode (S1S2=High-Low), then 64 pattern data and clock signals are sent via the backside flat cable. S1 and S2 are finally set to "stop shift" mode (S1S2=High-High), to keep the mask in memory if other cards have to be addressed.

This operation is repeated for each of the 27 RECV cards, unless a common mask is required for all the cards. The clock periods are set to 250 ns. In the usual operating mode, when the mask pattern is common to all cards (e.g. all gates open), it takes  $8 \mu s$  to load the cards in "shift left" mode and  $16 \mu s$  to set the mask patterns, within a crate. The total mask loading time is then  $\sim 24 \mu s$  for one crate and the three crates loading is thus done in  $\sim 72 \mu s$ .

## 6 Calibration and monitoring of the detector

### 6.1 General principles

The TRD separation method is based on the amount of charge deposited in the detector gas by different particles. As this deposited charge has rather large intrinsic fluctuations, its measurement by proportional tubes should bring the smallest possible additional uncertainties and needs precise calibration and control systems.

The deposited charge depends upon the track angle and position for a given particle. Complex processes involving space charge effects can also influence the charge collected at the wire level. The signal coming out of the charge ADC connected to each straw tube depends also on the response functions of the tube and of the electronic chain. The tube response depends upon the straw tube gain, which is a function of the gas composition, the high voltage, the

pressure and temperature in the straw. The electronic chain response depends mainly on the gain and linearity of the preamplifiers on the detector and of the receivers in the control room. This part of the response is controlled by a test-pulse calibration system.

Many parameters of the gain of the straw are controlled by a "Slow Control" system, without automatic feed-back.

The global response is calibrated permanently during data taking, at the mid-height of each straw, by a system using  $^{55}\text{Fe}$  radioactive sources. In addition, muons crossing the detector are used for monitoring over the full area of the detector.

The following paragraphs describe the different elements of the control and calibration processes.

### *6.2 The electronic gain control system*

Calibrated charges can be injected on the input stages of the preamplifiers by remote-controlled DAC's mounted on each front-end card. The system can address preamplifiers via a CAMAC 16-bit output register connected to a specific electronics module.

The electronic calibration system have been used to check the cabling and to measure periodically the linearity of the electronic chain as well as the cross-talk between channels. Non-linearities smaller than 1% and negligible cross-talk have been measured.

### *6.3 The Slow Control system*

The Slow Control system surveys the parameters defining the running conditions of the detector. The system generates alarms and records informations for off-line corrections every hour and for each alarm.

The differential pressure and temperature are measured at the bottom and top of each TRD plane (see Figure 3.1), and the absolute pressure is measured in the surround of the detector. By combining these measurements, the absolute pressure of each TRD plane can be determined with an accuracy of about 2 mbars. The temperature measurements have an accuracy of  $0.1^\circ\text{C}$ . In addition, the high voltage applied to each half-plane of the detector is measured with an accuracy of 10 volts by a simple resistive divider. The front-end electronics low voltage supply is also monitored. On each side of a TRD plane, a slow-control

card collects the probe signals and transmits them in the control-room to CAMAC Data Loggers linked to a dedicated computer. An interfacing program converts the probe signals and displays the results.

In the gas station, an hygrometer and an oxygen detector measure the water vapour and oxygen contamination which are kept below acceptable thresholds (about 400 ppm for water and 40 ppm for oxygen). A specific device measures the proportion of methane. Mass flowmeters measure the input of xenon and methane.

#### *6.4 Calibration with $^{55}\text{Fe}$ sources*

The absolute calibration of the detector is based on the measurement of the energy deposited by 5.89 keV X-rays emitted by  $^{55}\text{Fe}$  sources. Tapes impregnated by a  $^{55}\text{Fe}$  sulfate solution are attached horizontally across the middle of each straw plane, on the external envelope facing the straws. The source activity gives rise to about 20 counts/s per straw. The  $^{55}\text{Fe}$  sources serve also for the TRD monitoring.

##### *6.4.1 The calibration procedure*

During data taking periods, the TRD is continuously calibrated. Calibration triggers are enabled at each accelerator cycle during off-spill time and 256 calibration events are recorded in each ADC card, filling the memory depth of all the 64 ADC channels. The TRD on-line acquisition controller reads out each event and separates the values corresponding to the hit straw from the 63 pedestal values.

The  $^{55}\text{Fe}$  values are histogrammed for each straw and a gaussian fit is performed on the distributions at the end of a run. The mean and sigma values of the fits are saved in a database and define the  $^{55}\text{Fe}$  calibration values for a run.

Pedestal means  $\mu_{Ped}$  and widths  $\sigma_{Ped}$  used for the TRD calibration are obtained differently: during normal data acquisition, the data are recorded above a threshold of  $\mu_{Ped} + 5\sigma_{Ped}$ . Every 100 bursts, this zero-suppression is not carried out and recorded events contain pedestal data from all the straws. Fits are performed on these data to evaluate  $\mu_{Ped}$  and  $\sigma_{Ped}$  and the results for the run are sent to the database.

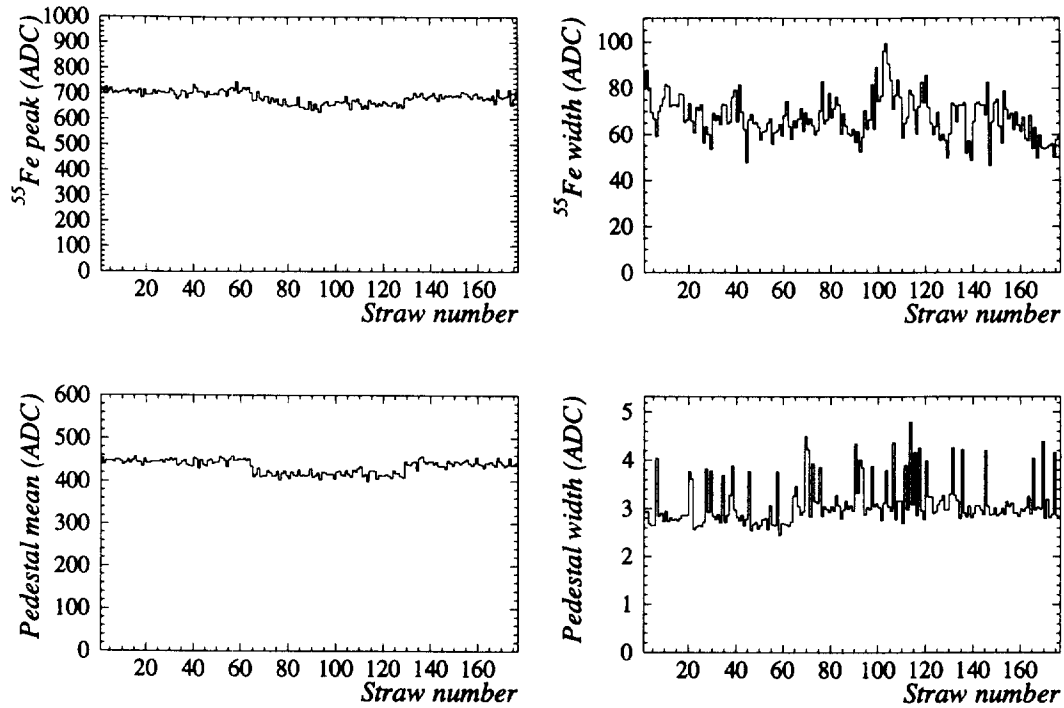


Fig. 6.1. TRD monitoring profiles of the 176 straws of a plane:  $^{55}\text{Fe}$  response peak (top left) and width (top right); pedestal mean (bottom left) and width (bottom right).

#### 6.4.2 $^{55}\text{Fe}$ monitoring

Histograms of  $^{55}\text{Fe}$  values and arrays containing means and widths of the pedestals from calibration events are sent every 10 minutes to the TRD on-line monitoring program. Summary histograms (as in Figure 6.1) of the calibration parameters are produced for on-line controls every few hours. On-line (and off-line) controls have actually shown that changes are very smooth. Pedestals are remarkably stable (variations are  $\leq 1$  ADC count/month). The main variations of the  $^{55}\text{Fe}$  values are connected with global parameter changes, such as gas composition or temperature.

#### 6.5 Monitoring with muons

The  $^{55}\text{Fe}$  sources provide monitoring of each TRD channel for a central position on the straw. A complementary method is used to obtain the response map on the whole surface of a TRD plane, as a function of altitude  $Y$  and lateral coor-



dinate  $X$  (i.e. the straw number). This method uses the fast-reconstruction, for each accelerator cycle, of about 50 muons tracks crossing the detector during the "flat top" period separating the two neutrino pulses. The extrapolation of muon chamber tracks gives the  $X, Y$  track positions in each TRD plane. In the horizontal projection, informations from matched TRD tracks are used to improve the precision in  $X$ .

The response uniformity can be checked as function of  $X$  and  $Y$  or in 2 dimensions ( $X, Y$ ). Muon tracks, mostly perpendicular to the planes, deposit the same energy in the straws irrespective of the position. This fact is used to detect the difference in gain both between straws and within individual straws. The muon average signal for  $|Y| \leq 15$  cm is used to normalize the signals.

At the time of the experiment setting-up, the gain was found higher near the bottom of the planes and lower near the top, due to excessive heat dissipation of the front-end electronics at the bottom and to an increasing gas contamination near the top. The electronics was modified and the gas flow was increased to cure the problems. Figure 6.2 shows the  $Y$  profile of the TRD response before and after the changes.

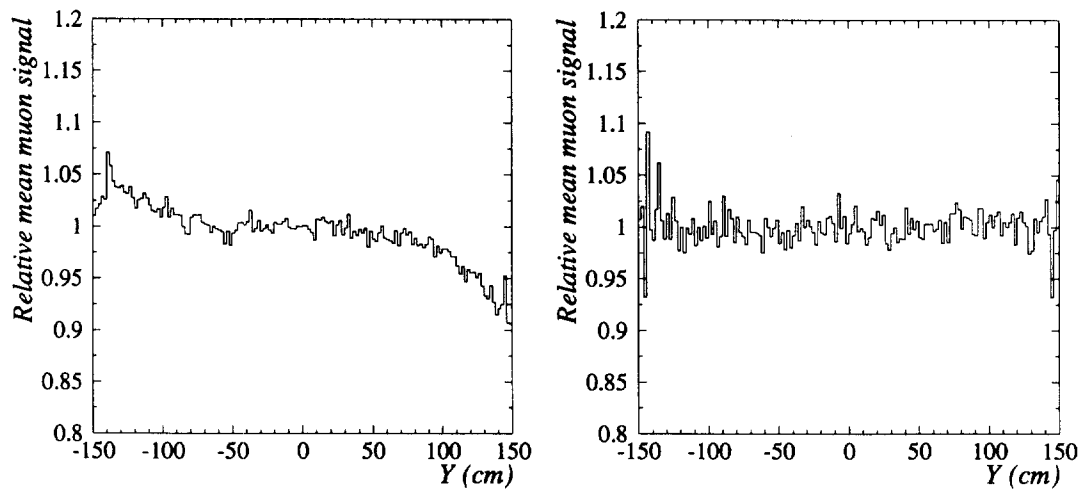


Fig. 6.2. Response to muons as a function of the altitude  $Y$ , relative to the straw center response, before (left) and after (right) detector adjustments. Larger fluctuations at both ends of the plots are due to low statistics.

After these modifications, the TRD response was shown to be uniform over the whole surface of the detector. Therefore, the  $^{55}\text{Fe}$  energy conversion factors are used without corrections.

## 7 Studies of the detector response

### 7.1 Tests of the straw response with radioactive sources

#### 7.1.1 Gain variation with various parameters

The variation of the response to a  $^{55}\text{Fe}$  source with high voltage HV, temperature T, pressure P,  $\text{CH}_4$  percentage and  $\text{N}_2$  contamination has been measured using a short straw prototype (10 cm long) fed through mass flowmeters, and equipped with pressure and temperature sensors. Results of the measurements are shown in Figure 7.1.

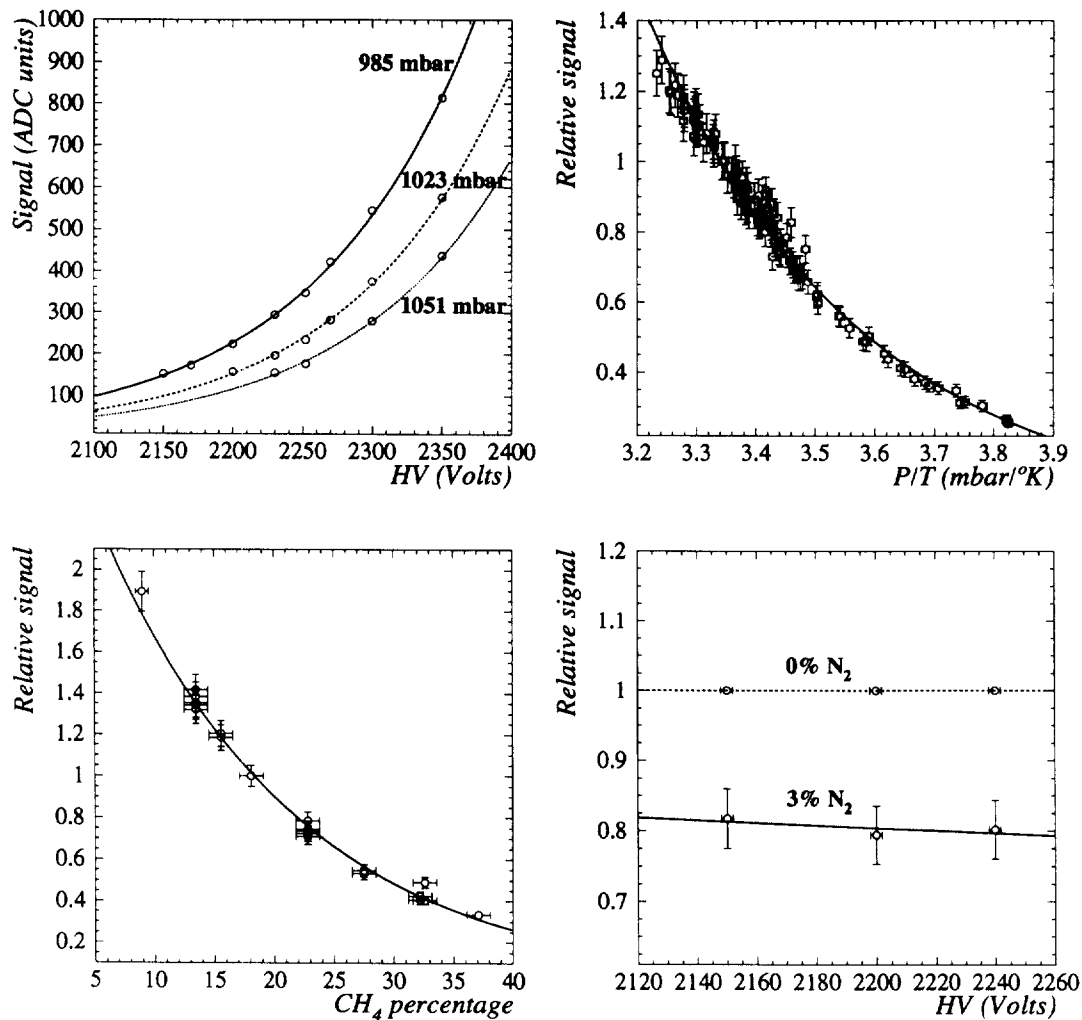


Fig. 7.1. Variation of the signal versus High Voltage (top left). Relative variation of the signal with  $P/T$  (top right), with  $\text{CH}_4$  percentage (bottom left) and in presence of a 3%  $\text{N}_2$  contamination (bottom right). Curves are exponential fits to the data.

For a 3% nitrogen contamination, the gain decreases by  $20.0\% \pm 4.7\%$ . The other variations of the gain are summarized in Table 4.

parameter	central value	gain variation
H.V.	2250 Volts	+0.87%/Volt
temperature	25°C	+2.8%/°C
pressure	1020 mbar	-0.93%/mbar
CH <sub>4</sub> percentage	20%	-6.2%/CH <sub>4</sub> %

Table 4  
Gain variation with different parameters.

### 7.1.2 Saturation effects

With the same prototype, the linearity of the output signal with the deposited energy has been measured using low rate X-ray sources at 7 discrete energy values between 5.89 and 44.2 keV. Figure 7.2 shows the measured signal versus photon's energy at 2250 V, 30°C, 1019 mbar and 18% CH<sub>4</sub>. A saturation effect is observed, which is interpreted as mainly due to space charge effects. The deviation from linearity is about 35% at 22 keV, if one takes as the unsaturated response function the tangent at the origin of the fitted exponential curve. The corresponding saturation of the <sup>55</sup>Fe signal is 8.7%.

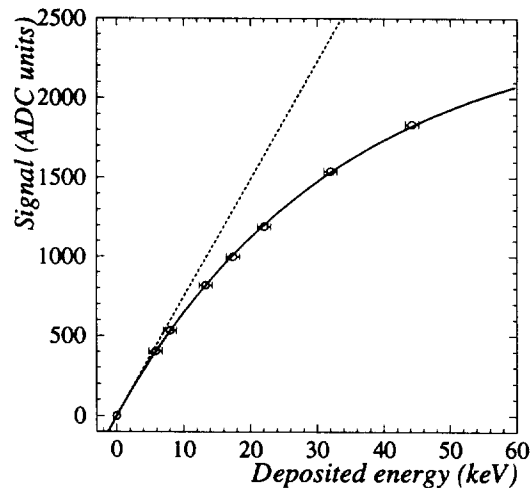


Fig. 7.2. Measured signal versus photon's energy.

### 7.2 Tests of the detector with beam particles

Checks were performed with test-beams of electrons and pions at various particle momenta between 1 and 10 GeV/c, first on prototypes, and later on

modules of the final detector to assess the production of transition radiation and the response of the detector. Figure 7.3 shows the signal obtained using a single TRD module with 10 GeV/c electrons and pions at normal incidence. Parameters such as the particle angle of incidence and impact point were also varied.

The test-beam results were used to cross-check the simulation of the detector, which led to the particle identification algorithms [12]. Together with the calculation of the transition radiation, the simulation programs [9] include a special parametrisation from Ermilova et al. [13] for the  $dE/dx$  deposition in thin layers of gas.

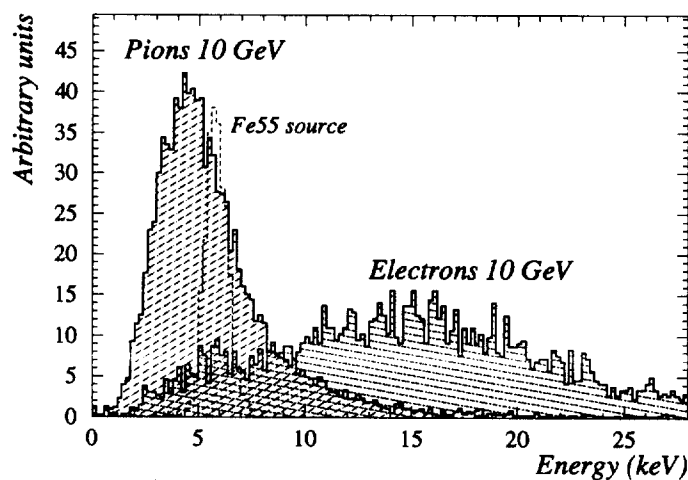


Fig. 7.3. Response of a full-size TRD module to test-beam particles

### 7.2.1 Uniformity of the radiators

The production of transition radiation could vary due to differences in gap uniformity across the radiator area. The impact point on the radiator was therefore varied. The mean signal with electrons was found to be constant within 5% for large as well as small step scans across the area.

Differences in the photon yield between radiators could be expected as the spacing uniformity was improved after the construction of the first four, by increasing the height of the bumps made in the film surface from 200 to 250  $\mu\text{m}$ . The first four TRD modules are placed in the downstream position within the module doublets to compensate their lower photon yield by the detection of unabsorbed photons from the upstream module. Tests performed during the experiment, and described in another paper [12], have not exhibited significant differences in the response of modules to electrons.

### 7.2.2 Effects of the track angle

Simulation studies [9] have shown that the increase of the TR photon yield due to a non-zero track angle of incidence (enlarging the foil thickness and spacing crossed by the particle) is compensated by the larger absorption in the radiator for small angles.

On the other hand, the  $dE/dx$  part of the signal can change with the angle of incidence of the track in the vertical plane. This effect was measured in the experiment, using the flux of muons traversing the detector during the "flat-top" period between the two neutrino bursts of the SPS. As muon momenta range from 3 GeV/c to 50 GeV/c, the signals are corrected to take off the effect of the  $dE/dx$  relativistic rise. The effect on the track path of the vertical angle are also removed. The high-voltage was 2300 Volts. The results are shown in

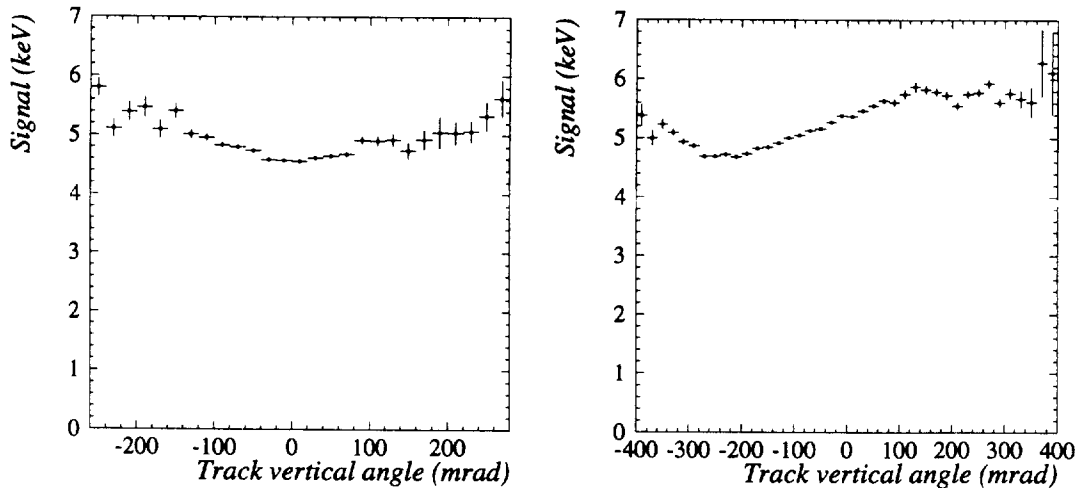


Fig. 7.4. Muon signal versus vertical angle without (left) and with magnetic field (right).

Figure 7.4 with no magnetic field and with the magnetic field set to its normal value of 0.4 Tesla.

The decrease of about 17% at 0 mrad when the field is off is interpreted as a space charge effect, as the drift electrons are collected at the same location when the track is perpendicular to the wire. When the field is on, the drift electrons are focused at a single location on the wire when the track angle is about  $-200$  mrad. During data taking, in order to decrease the amplitude of the effect, the high-voltage was lowered from 2300 Volts to 2225 Volts. The effect is reduced from 17% to 12%.

### 7.2.3 Effect of the track distance from the straw center

The variation of the signal with the track distance from the straw center was measured in a 6 GeV/c pion-electron test beam with a 50 cm straw and a small prototype radiator. The beam was perpendicular to the straw axis. The

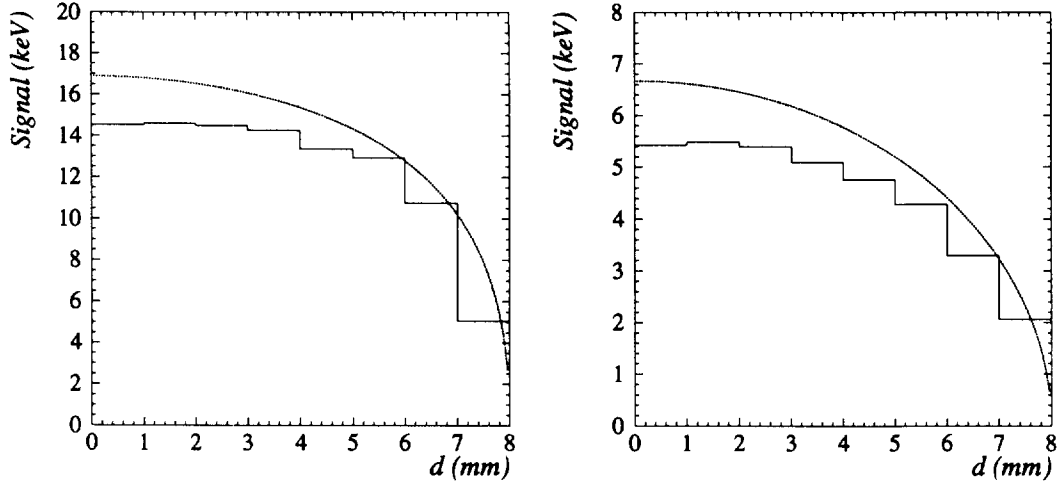


Fig. 7.5. Signal of a TRD prototype in a 6 GeV/c test beam versus the track distance  $d$  to the straw axis for  $e^-$  (left) and  $\pi^-$  (right). Note the different vertical scales. Curves are estimates of the unsaturated signals (see text).

conditions were the same as in the final detector operated at 2300 Volts (the wire diameter was  $20 \mu\text{m}$ ) and the high-voltage 1800 Volts, resulting in the same gain). The result is shown in Figure 7.5 as a function of the distance  $d$  from the track to the straw wire.

The electron signal at  $d=6.5$  mm (leaving aside the low-statistics last bin at  $d=7.5$  mm) amounts to  $\sim 2/3$  of the signal at the center. This is more than one would expect, if variations were only due to the differences in path length. This difference is interpreted as due to space charge saturation effects. The curves in Figure 7.5 come from a simplified calculation of the unsaturated signal, using the results given in the previous sections on the saturation measured with muon tracks and with photons of different energies. For electrons, unsaturated signals from TR and  $dE/dx$  are supposed to just add together. The saturation effects due to  $dE/dx$  ionization losses are found to be stronger than those caused by X-ray photons.

The effects on the detector signal of the track angle and distance to the wire, although reduced by the decrease of the high-voltage adopted for the data-taking, are still important. In the identification of a particle track of given position and angle, these effects are cancelled at first order. Analyses of the performances of the detector on real data [12] constitute a justification of this hypothesis.

## 8 Conclusion

We have designed and constructed for the NOMAD experiment a large area Transition Radiation Detector system to identify electrons at 90% efficiency with a rejection factor against pions of  $10^3$ . Although made of very thin material extending over large dimensions, the detector has proven to be robust. The detector has now been operating for more than three years and works with excellent stability. A single straw, out of a total of 1584, has become partially inefficient due to a loss of tension in the wire.

First studies using pion and electron test beam measurements on single modules of detector showed that the expected rejection level was reached, thanks to the quality of the detector. The performance of the NOMAD transition radiation detector has been further ascertained over the particle momentum range of 1 to 50 GeV/c using data recorded during the experiment. Another paper [12] describes the algorithms developed for electron identification, and the tests on real data which demonstrate the achieved identification performances.

## Acknowledgments

We would like to thank A. Beer, G. Gallay and J. Mulon from CERN-PPE for their help in the detector installation at CERN, C. Girard /LAPP for his advices on the mechanical design and construction of the detector, M. Bosteels-/CERN-MT and D. Fromm/CERN-PPE for their help in the elaboration of the gas system, and M. Dialinas/LAL-Orsay for helpful discussions on the materials. We are also grateful to P. Farthouat and C. Sobczynski for their role in the realisation of the Fastbus ADC cards, to G. Roubeau/CERN-TIS for his help on the radioactive sources used for detector calibration, and to A. Lutke/CERN-PPE for drawings of the radiator construction.

## References

- [1] The NOMAD Collaboration, P. Astier *et al.*, "Search for the oscillation  $\nu_\mu \rightarrow \nu_\tau$ ", CERN-SPSLC/91-21, CERN-SPSLC/91-48, CERN-SPSLC/91-53, CERN-SPSLC/93-31.
- [2] The NOMAD Collaboration, J. Altegoer *et al.*, "The NOMAD experiment at the CERN SPS", Paper submitted to Nucl. Instr. and Meth.

- [3] For an overview of transition radiation detectors, see for example B. Dolgoshein papers [8] and references therein, and S. Paul, "Particle identification using transition radiation detectors", CERN report PPE 91-199 (november 1991).
- [4] V.L. Ginzburg and I.M. Frank, *Z. Eksper. Teor. Fiz.* 16 (1946) 15.
- [5] G.M. Garibian, *JETP* 6 (1958) 1079;  
G.M. Garibian, *JETP* 10 (1960) 372;  
K.A. Barsukov, *JETP* 10 (1960) 787.
- [6] X. Artru, G.B. Yodh and G. Mennessier, "Practical theory of the multi-layered transition radiation detector", *Phys. Rev. D* 12 (1975) 1289.
- [7] G.M. Garibian, L.A. Gevorgian and C. Yang, "The calculation of X-ray transition radiation generated in regular- and irregular-layered media", *Nucl. Instr. and Meth.* 125 (1975) 133.
- [8] B. Dolgoshein, "Transition radiation detectors and particle identification", *Nucl. Instr. and Meth.* A252 (1986) 137;  
B. Dolgoshein, *Nucl. Instr. and Meth.* A326 (1993) 434.
- [9] T. Fazio, "Le détecteur à rayonnement de transition de l'expérience NOMAD pour l'identification du  $\tau$  dans le canal  $\tau^- \rightarrow e^- \bar{\nu}_e \nu_\tau$ ", Doctorate thesis, University J. Fourier - Grenoble I (1995).
- [10] A. Peisert and F. Sauli, "Drift and Diffusion of Electrons in Gases: a Compilation", CERN report CERN/84-08 (1984);  
L.G. Christophorou *et al.*, *Nucl. Instr. and Meth.* 171,(1980),491.
- [11] The NOMAD straws were manufactured by Lamina Dielectrics Ltd. (England).
- [12] G. Bassompierre *et al.*, "Performances of the NOMAD Transition Radiation Detector", to be submitted to *Nucl. Instr. and Meth.*
- [13] V.C. Ermilova, L.P. Kotenko and G.I. Merzon, "Fluctuations and the most probable values of relativistic charged particle energy loss in thin gas layers", *Nucl. Instr. and Meth.* 145 (1977) 555.